From CO₂ emissions to atmospheric NO₂ mixing ratios: simulating chemical processes and their impacts on TROPOMI retrievals over the Middle East

Ioannis Cheliotis[1], Thomas Lauvaux[2], Jinghui Lian[3], Theodoros Christoudias[4], George Georgiou[4], Alba Badia[5], Frédéric Chevallier[1], Pramod Kumar[1], Yathin Kudupaje[1], Ruixue Lei[6], Philippe Ciais[1,4]

[1]Laboratoire des Sciences du Climat et de l'Environnement (LSCE), IPSL, CEA-CNRS-UVSQ, Université Paris-Saclay, 91191 Gif sur Yvette Cedex, France
[2]Groupe de Spectrométrie Moléculaire et Atmosphérique (GSMA), Université de Reims-Champagne Ardenne, UMR CNRS 7331, Reims, France
[3]SOUEZ, Le Pecq, France
[4]Climate & Atmosphere Research Center, The Cyprus Institute, Nicosia, Cyprus
[5]Sostenipra Research Group, Institute of Environmental Sciences and Technology, Universitat Autònoma de Barcelona, 08193 Bellaterra, Barcelona, Spain
[6]Environmental Health and Engineering, Johns Hopkins University

Correspondence to: Ioannis Cheliotis (ioannis.cheliotis@email.com)

Abstract. As many large metropolitan areas have pledged for a rapid decrease of their greenhouse gas emissions through ambitious climate mitigation policies, the need for rapid and robust quantification methods became more pressing. At the global scale, the scarcity of satellite carbon dioxide (CO_2) observations remains the major roadblock to producing independent city-scale CO_2 emissions estimates from atmospheric data, except for a handful of cities benefiting from a dense network of ground-based CO_2 sensors. In this study, we quantify the potential of assimilating indirect measurements from spaceborne sensors (here nitrogen dioxide - NO_2) to constrain fossil fuel CO_2 emissions, relying on the co-emission of these two species during combustion. We developed a modeling framework using a NO_x-aerosol chemistry transport model (WRF-Chem) and performed simulations of NO_2 and CO_2 over the Middle-East, an area known for its large cities, its frequent clear sky conditions and a fairly constant albedo from its desertic land. We first demonstrate the importance of production/destruction processes impacting NO_2 lifetime at short and long distances from the source, suggesting that simplified approaches may be impacted by large errors. In comparison to TROPOMI satellite observations, the simulated NO_2 plumes from emissions inventories (EDGAR) revealed large misattribution of NO_2 emissions at fine scales, hence an uncertain disaggregation of national emissions to single point sources in the industrial and energy sectors in the EDGAR inventory. We further studied the relationship between NO_2 and CO_2 during summer and winter seasons by simulating the enhancement ratios ($\delta NO_2:\delta XCO_2$) in plumes produced by cities and point sources We found that the enhancement ratios are consistent with the observed ratios derived from the ESA TROPOMI (NO_2) and NASA OCO-3 missions (XCO_2). We conclude here that the spatial misattribution of NO_2 emissions parallels the misattribution of CO_2 emissions, and that improved NO_2 inventories could therefore be used to

improve the monitoring of CO_2 emissions at sub-national scales in current global inventories when a sufficiently-large amount
35 of NO_2 satellite measurements are available.

1 Introduction

The increase in global fossil fuel emissions reached about 1 % in 2022 with large variations at the regional level (Friedlingstein
et al., 2022). The two most commonly used approaches for estimating fossil fuel emissions are inventories (bottom-up) and
atmospheric inversions (top-down; Enting et al., 1998). While inventories remain the primary source of information at national
40 scale (Smith et al, 2022), inverse modeling techniques have increasingly informed policy makers and governments of
unreported sources and natural sinks across the globe (Yu et al, 2023). Because bottom-up approaches rely on uncertain
emission factors and activity data across various sectors of the economy, large errors and uncertainties have been documented
at regional and local scales for CO_2 (Andres et al. 1996; Oda et al., 2019) but also for CO and NO_x (Elguindi et al, 2020).
Commonly used bottom-up emission inventories such as the Emissions Dataset for Global Atmospheric Research (EDGAR;
45 Janssens-Maenhout et al, 2015) including various gases such as NO_x, CO_2 and VOC for the entire globe (Crippa et al, 2020),
the Copernicus Atmosphere Monitoring Service regional scale (CAMS-REG) including various chemical species (Kuenen et
al, 2021) or the Open-Data Inventory for Anthropogenic Carbon dioxide (ODIAC) providing globally CO_2 emissions from
fossil fuel combustions (Oda and Maksyutov, 2011) have provided gridded emissions estimates that can be combined with
ground-based or satellite atmospheric measurements of greenhouse gases to perform atmospheric inversions (Lauvaux et al.
50 2016; Staufer et al. 2016; Yadav et al., 2021). But the limited number of atmospheric station networks continuously measuring
GHG concentrations limits our ability to perform atmospheric inversions over most regions of the globe (Peylin et al, 2013).
Even satellite missions measuring CO_2 concentrations such as the NASA Orbiting Carbon Observatory (OCO-2; Crisp et al.,
2017) or the JAXA GOSAT mission (Yokota et al., 2009) only collect a sparse and infrequent set of measurements at sub-
national scales (Chevallier et al, 2017). The NASA Orbiting Carbon Observatory-3 (OCO-3) (O'Dell et al, 2018; Taylor et al,
55 2023) mission offers a Snapshot Aera Mode (SAM) capturing partial images of XCO_2 concentrations few times a year over a
selection of large cities and power plants across the world. However, most inverse studies assimilating OCO-3 measurements
have not been able to monitor and to assess urban-scale emissions at policy-relevant scales (e.g. Ye et al., 2020; Kiel et al.,
2021; Roten et al., 2022).
Since its launch in 2017, the Tropospheric Monitoring Instruments (TROPOMI) provides daily images of tropospheric NO_2
60 column measurements over the entire globe, part of the European Union's Copernicus Sentinel 5 Precursor (S5p) satellite
mission (Copernicus Sentinel-5p, 2021) at 5 to 7 km resolution. Co-emitted during the combustion process of fossil fuel energy,
NO_2 and CO_2 have been jointly studied to quantify fossil fuel emissions of CO_2 at fine scales (e.g. Hakkarainen et al, 2021;
Kuhlman et al, 2020). The estimation of the NO_2:CO_2 ratios remains uncertain, highly dependent on the activity sectors (Lei
et al., 2022). Other studies have simply used NO_2 plumes from TROPOMI to assist in the detection of CO_2 plumes obscured
65 by the high background CO_2 values (Reuter et al, 2019). The precise detection and quantification of NO_x emissions from large

point sources has also been studied over multiple cities using Gaussian models to represent the atmospheric dispersion of pollutants (Wu et al, 2021). Yang et al (2023) have recently showcased a methodology to derive CO_2 emissions from NO_2 fields by using GEOS-Chem model, however they did not consider the chemical reactions in their methodology which could be a major issue for the correct simulation of NO_2 concentrations. The performance of atmospheric chemical models with

70   regards to chemical and transport processes can lead to significant errors in emissions estimates (Stavrakou et al, 2013). The Weather Research and Forecasting (WRF) model (Skamarock and Klemp, 2008) coupled with its chemistry module (WRF-Chem, Grell et al, 2005; Fast et al, 2006) has been developed for studying atmospheric pollution, applied to top-down approaches (e.g. Georgiou et al, 2018) and coupled to bottom-up emissions estimates (Goldberg et al, 2019). The main advantage of utilizing an atmospheric model is the ability to simulate gas concentrations at high spatial and temporal

75   resolutions while simulating the full complexity of chemical processes (e.g. Zhang et al, 2012; Sicard et al, 2021). From the comparison of the simulated NO_2 and CO_2 concentrations with satellite observations, it is possible to examine the emission inventories coupled to the atmospheric model for NO_2 (e.g. Luna et al, 2020) and for CO_2 (Kiel et al, 2021).

Regarding the complex NO_x chemistry, NO to NO_2 concentrations rapidly vary depending on ozone (O_3) concentrations and the presence of Volatile Organic Compounds (VCs) that control OH radicals. Most combustion processes emit primarily NO

80   molecules, converted into NO_2 within minutes after their release. Satellites only observe NO_2 columns, hence matching model simulations with satellite observations requires the use of a chemical transport model. The simulation of the conversion rate of NO to NO_2 (and inversely) remains highly uncertain due to nonlinear chemical processes, as described in Atkinson (2000) and Seinfeld and Pandis (2006). The most common pathway for the conversion of NO to NO_2 occurs via oxidation by ozone (O_3). This conversion occurs on the order of tens of seconds to a few minutes and depends on the amount of available reactants,

85   such as O_3 and VOCs, the intensity of solar radiation, as well as ambient meteorological conditions. However, during late afternoon and evening hours, high O_3 concentrations are observed in remote locations due to less titration by NO, and transport of O_3 and its precursors from their sources. At nighttime, without photolytic activity, and near very large emissions of NO (e.g. power plants), NO react with O_3 to form NO_2, which subsequently produces nitric acid (HNO_3) removed by wet and dry deposition (Monks et al., 2015). The complex chemistry of NO and NO_2, and hence the relationship between CO_2 and NO_2,

90   requires the careful evaluation of the chemical transport model before using NO_2 concentrations to constrain CO_2 emissions. The aim of the current study is to address the ability to identify large NO_2 and CO_2 plumes over the Middle-East region by implementing the WRF-Chem model and comparing its outputs with satellite observations from TROPOMI and OCO-3 respectively, in the framework of the Eastern Mediterranean and Middle East - Climate and Atmosphere Research (EMME-CARE) project. The Middle East region is characterized by large emitters, an energy system based on fossil fuels, high energy

95   consumption per capita, high-power demand due to high temperatures during the hot season and heavy industrial activities. Moreover, it is a region with an abundance of clear sky days throughout the year and a rather constant albedo which benefits satellite observations (Eskes et al, 2022). For the anthropogenic emissions inputs applied to the model, the EDGAR inventory was selected and provided data for the entire area of interest. Different emissions sectors were considered (from EDGAR) such as energy production, whose emissions come from large point sources (power plants), ground transportation, residential and

100 industries, all corresponding to different NO_2-to-CO_2 ratios. We examine the model performances in simulating the NO_2-to-NO (and vice-versa) conversion rates for individual plumes across the Middle East, before analyzing NO_2-to-CO_2 ratios and our ability to assimilate NO_2 column measurements to estimate CO_2 fossil fuel emissions. The methodology, WRF-Chem set-up and tools utilized for this study are presented in Section 2. Section 3 demonstrates the performances of WRF-Chem when simulating NO_x, with and without chemistry, along with the comparison between the model and satellite observations of the

105 δNO_2:δXCO_2 enhancement ratios. Finally, Section 4 summarizes the key points of the study.

2 Methodology

2.1 WRF-Chem set up

The Weather Research and forecasting (WRF) model with chemistry module (WRF-Chem) version 3.9.1 (Skamarock and Klemp, 2008) was used for the simulation of the greenhouse gases over the Middle East region for the months of June and

110 January 2021. Our study area encompasses several large cities including Riyadh, the capital and largest city of Saudi Arabia, Doha, capital and largest city of Qatar, and Dammam. The parent domain is about 2,000 km wide (139 by 139 grid points) at 15 km spatial resolution, and the child domain (one-way nesting) is about 700 km wide (231 by 231 grid points) at 3 km spatial resolution, as shown in Fig. 1.
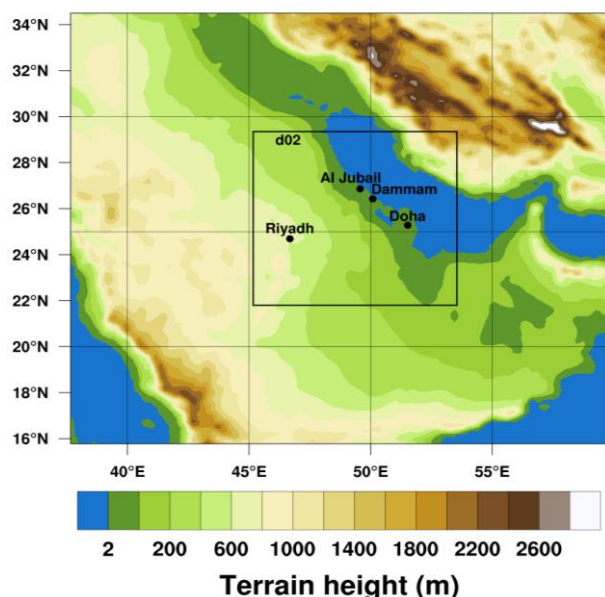
115

Figure 1: WRF-Chem simulation domains at 15-km and 3-km resolutions, respectively, over the Middle-East and terrain height (in meter), using one-way nested mode.

Regarding the WRF-Chem schemes options, we selected a configuration from previous studies of the atmospheric pollution over the Middle East and the Eastern Mediterranean region (Zittis et al 2014; Georgiou et al, 2022). The atmospheric column was represented by 33 vertical levels for both domains. The land surface energy exchange was simulated using the Noah Land-Surface Model scheme (Chen and Dudhia, 2001), while the Planeteray Boundary Layer dynamics was simulated using the Yonsei University (YSU; Hong et al, 2006) planetary boundary scheme. For the chemistry scheme, the Carbon Bond Mechanism version Z (CBM-Z, Zaveri and Peters, 1999) was preferred for its better performances in terms of NO_x concentrations (Visser et al, 2019) in combination with the Madronich TUV photolysis scheme (Madronich, 1987; Tie et al, 2003). The main schemes and options are described in Table 1.

Table 1: The basic options for the WRF-Chem setup.

Domains	Period under study	Spatial resolution	Temporal resolution	Chemistry
Parent: 139x139 *Nested: 231x231*	*June & January 2021*	*Parent: 15x15 km* *Nested: 3x3 km*	*1 hour*	*cbm-z*
Emissions	**Boundary layer**	**Surface physics**	**Cumulus**	**Microphysics**
cbm-z mosaic	*YSU*	*Noah Land-Surface model*	*Grell-Devenyi*	*Morisson 2-moment*
Shortwave radiation	*Longwave radiation*	**Photolysis**		
CAM	*CAM*	*Madronich TUV photolysis*		

For a simple model validation of wind fields, we compared the wind speed at 10 meters above ground level with the available METAR observations (Iowa Environmental Mesonet) at the two operational stations of Riyadh and Dammam airports. As shown in Fig. 2, monthly averages (January and June 2021), for January 2021, at the Riyadh airport station from 00:00 UTC until 10:00 UTC agree within <1 m s⁻¹ when the wind speed ranges from 2 m s⁻¹ to 4 m s⁻¹, while the WRF model overestimates the wind speed by approximately 2 m s⁻¹ from 12:00 UTC to 21:00 UTC, during low wind speed conditions. For June 2021, the WRF model agrees with the observations for the period 06:00 UTC to 15:00 UTC within 0.5 m s⁻¹, while overestimating wind speed for the time periods 00:00-03:00 UTC and 18:00-21:00 UTC, during low wind speed conditions. On the other hand, at the Dammam airport station, the WRF model tends to underestimate wind speed during January 2021 for the time period 06:00-12:00 UTC by approximately 1-2 m s⁻¹, and to overestimate wind speed at 00:00 and 21:00 UTC by 1 m s⁻¹. During June 2021, the WRF model tends to underestimate wind speed at 03:00 and 06:00 UTC by 1-2 m s⁻¹, but overestimates wind speed at 12:00, 15:00 and 21:00 UTC by approximately 1 m s⁻¹.
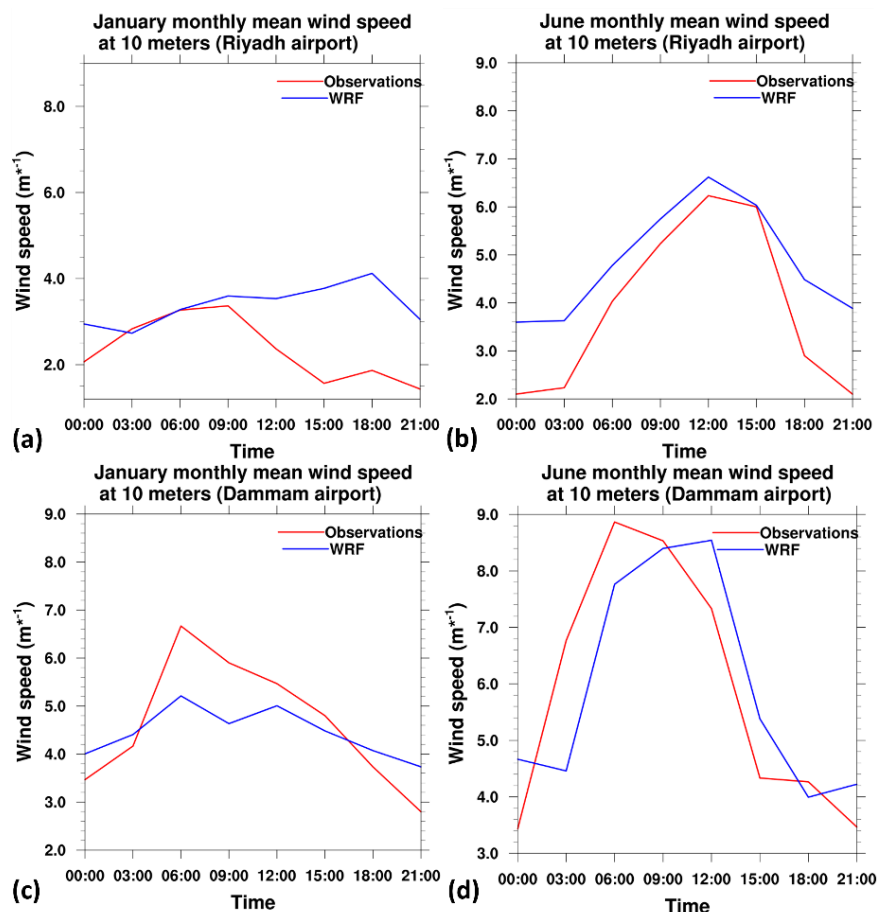
Figure 2: Modeled and observed monthly mean wind speed (m/s) at 10 meters for the months of January (left column) and June (right column) 2021 over Riyadh (top row) and Dammam (bottom row) airports.

The EDGAR-htap v2.2 emission dataset (Joint Research Centre Data Catalogue, 2017) was coupled to the WRF-Chem model to simulate the anthropogenic concentrations. It is important to note that the dataset providing all the necessary gases for the

140

145 NO_x simulation is based on 2010 data. Later versions of the EDGAR inventory, up to the time of the study, do not include important species required to simulate NO_x, most notably non-methane volatile organic compounds (NMVOCs) for the NO_x simulations. The EDGAR-htap v2.2 data are categorized in 5 different sectors: energy, industry, residential, and traffic, and air/shipping transportation (vehicles, airplanes and ships). Fig. 3 shows the contribution of each sector to the total NOx emissions as a ratio of the sums of the NOx emissions within the nested domain (Fig. 1) for each sector over the total sum of

150 the emissions from all sectors. The energy sector is the main contributor to the NO_x emissions in the area for January and June 2010 with 69 % of the total, followed by the industry and ground transportation sectors (around 14 %). The air transportation contributes to 1.9 % of the total emissions, and the residential emissions to 0.3 %. Fig. 3 shows the results for January 2010, overall similar to June 2010.
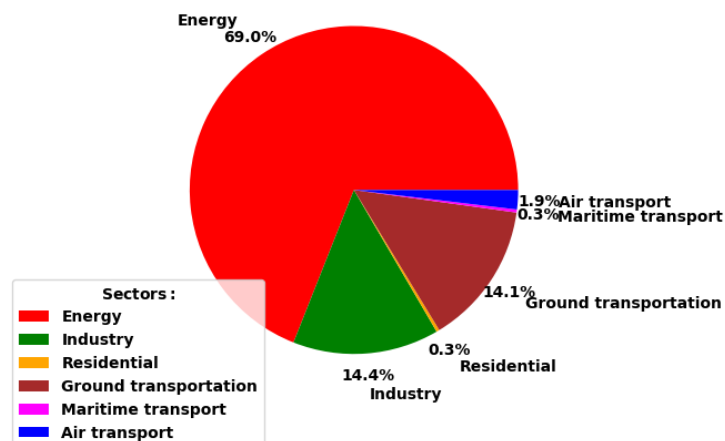
Figure 3: Contribution of the different energy sectors to the total NO$_x$ emissions for the nested domain of the study (Fig. 1) based on the EDGAR emissions inventory for January 2010.

Considering the CO$_2$ emissions, the EDGAR Greenhouse Gas Emissions (ghg) version 6.0 dataset of 2018 (Joint Research Centre Data Catalogue, 2021) was preferred (Monforti Ferrario et al., 2021). Because CO$_2$ is not reacting with other atmospheric species, we selected a later version to compare and to diagnose any changes in the point source locations compared to the EDGAR htap v2.2 dataset. In addition, the CO$_2$ EDGAR dataset consists of emissions from 18 sectors: energy, agriculture, industry, iron production, non-energy fuels, non-ferrous metals, non-metalic minerals, chemicals production, fossil fuel fires, fuel production, other products, residential, oil refineries, soil waste and transportation (vehicles, airplanes and ships). Fig. 4 displays the contribution of the different sectors to the total CO$_2$ emissions similarly to Fig. 3. However, the results show a strong seasonal variability in the energy sector contributing to 38.7 % of the total emissions, followed by the industry sector with 16 %, the oil refineries with 13.9 %, the ground transportation with 12.6 %, the chemicals production with 8.1 % and the rest of the sectors amounting to 10.4 % in January 2018. These results are quite different compared to June 2018, where the energy sector is contributing to 61.9 % of the total emissions, followed by the ground transportation sector with 10.3 %, the industry with 9.9 %, the oil refineries with 6.7 %, the chemicals production with 4.9% and the remaining sectors accounting for 6.3 %.
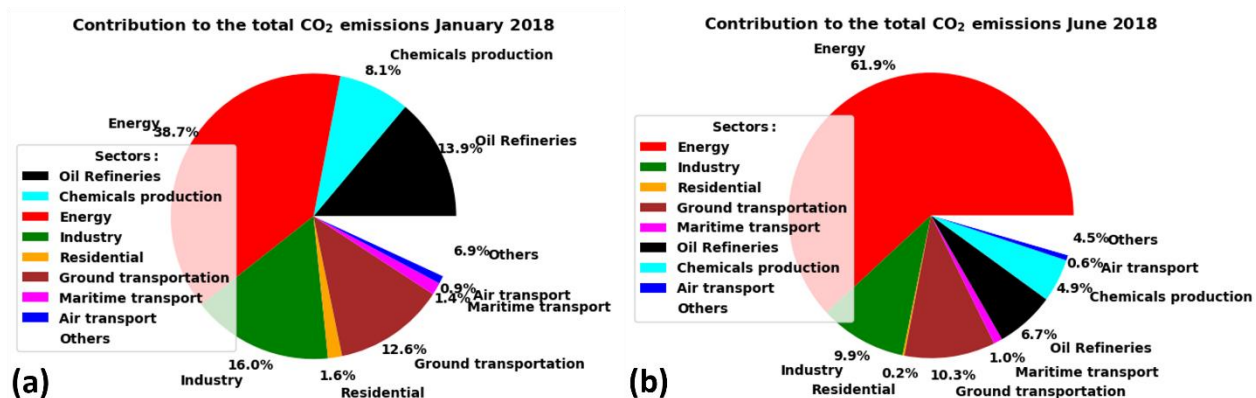
170

Figure 4: Contribution of the different energy sectors to the total CO2 emissions for the nested domain of the study (Fig. 1) based on the EDGAR emissions inventory for January and June 2018.

The EDGAR datasets provide emissions for the general molecular form of the various species (e.g. NO_x, Black Carbon, Organic compounds). Table A1 displays the relationships between the gas forms provided by EDGAR and how they should

175 be converted into WRF-Chem emissions species before being coupled to the chemistry module according to the WRF-Chem 3.9.1.1. emissions guide (2018). A recent study from Rey Pommier et al (2023) has produced a detailed infrastructure map with the known locations of the power plants and factories over the Middle East region, with 62 emitting sites in total. We show in Fig. 5 the locations of power plants and factories over the EDGAR-htap v2.2 NOx and EDGAR-ghg v6.0 emissions maps from the energy sector to unveil possible deficiencies of the energy point sources in the EDGAR datasets for our nested

180 domain. The EDGAR NO_x emissions lack some of the point sources along the Saudi Arabian and the Qatarian coastlines as well as near the city of Riyadh (cf. Fig. 5(a)).
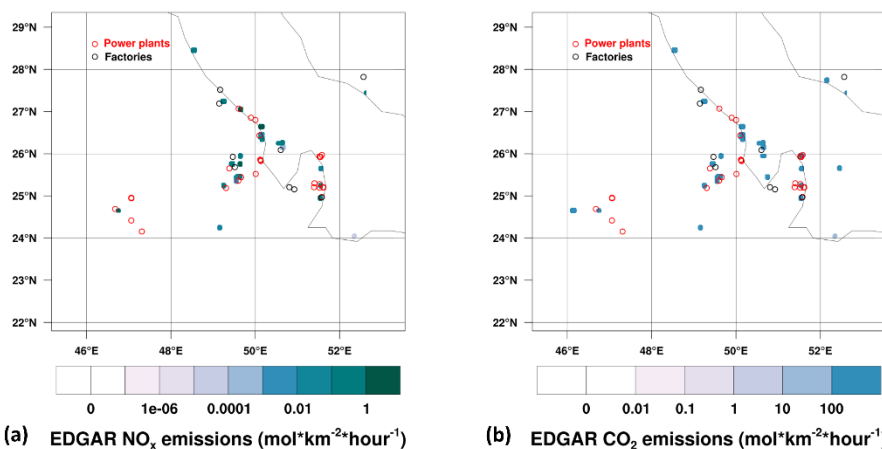
Figure 5: EDGAR NO_x monthly mean emissions for June 2010 (a) and CO_2 monthly mean emissions for June 2018 (b) solely for the energy sector along with the locations of the power plants and factories compiled (Rey Pommier et al, 2023) for the nested domain
185 **(Fig. 1). The power plants and factories with no values for EDGAR emissions reveal the missing sources of the inventory.**

Furthermore, the EDGAR datasets provide a mean diurnal profile of emissions for each month without considering the weekly and diurnal variability. Hence, we considered diurnal and weekly variations by estimating a scaling factor of EDGAR's profiles based on the energy consumption for Saudi Arabia, taking into account the seasonal variability as well as weekends (Friday and Saturday) (Al Ghamdi, 2020). We applied these scaling factors to generate hourly emissions over the region. The values for the scaling factor are presented in Fig. 6, with values ranging from 0.9 to 1.15, while weekly and seasonal cycles remain limited in peak-to-peak amplitude (0.2 to 0.3).
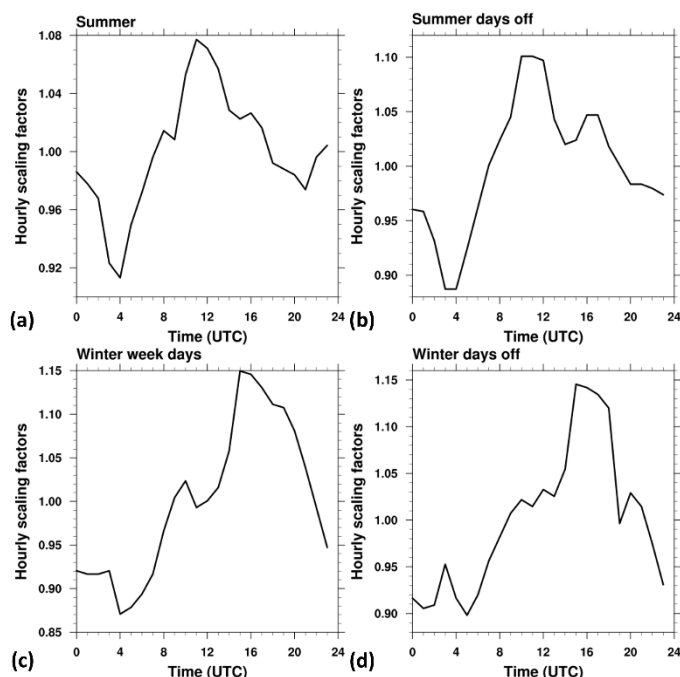
Figure 6: The hourly scaling factors for the parent and nested domains (Figure 1) in summer week days (a), summer days off including rest days on Fridays (b), winter week days (c) and winter days off (d) for January and June 2021, applied to the EDGAR emissions to include diurnal variability and estimated based on the electricity consumption in Saudi Arabia.

2.2 Satellite observations

The model outputs for January and July 2021 were compared against satellite observations. In particular, the simulated δNO_2 (see Section 3.3) were compared against the TROPOMI observations and the simulated δXCO_2 (see Section 3.3) against the NASA OCO-3 XCO_2 retrievals in SAM mode (see Fig. 10, 13, 14, 15). We collected a daily TROPOMI image sampled at approximately 10:00 UTC for the periods January 2021 and June 2021. The NO_2 data were downloaded from the European Space Agency (ESA) for the European Union's Copernicus Sentinel 5 Precursor (S5p) satellite mission (Copernicus Sentinel-5p, 2021). We note here that potential biases in TROPOMI NO_2 retrievals have been documented over large metropolitan areas Judd et al (2020). Regarding the evaluation of δXCO_2, we used the NASA OCO-3 observations from the NASA Goddard Earth Science Data and Information Services Center (GES 184 DISC) (http://disc.sci.gsfc.nasa.gov/). Only few partial images

205 with a sufficient number of quality-flagged retrievals (the retrievals cover the urban areas) are available over the region for the months of January and June 2021, mainly over the cities of Riyadh and Dammam. The full list of days collected by OCO3 are shown in Fig. A1.

Regarding the TROPOMI satellite data, Fig. 7 presents the fraction of days for each pixel where the quality factor is higher than 0.75. It is apparent that for June 2021, the fractions for the vast majority of the pixels are more than 80% with some

210 exceptions near the Saudi Arabian coastline and the Qatar coastline where the fractions decrease to approximately 70%, down to 60% for some pixels. During January 2021 the fractions for most of the pixels range from 70% to 80%, with some pixels in Saudi Arabian coastline and the Qatar coastline dropping below 40%.
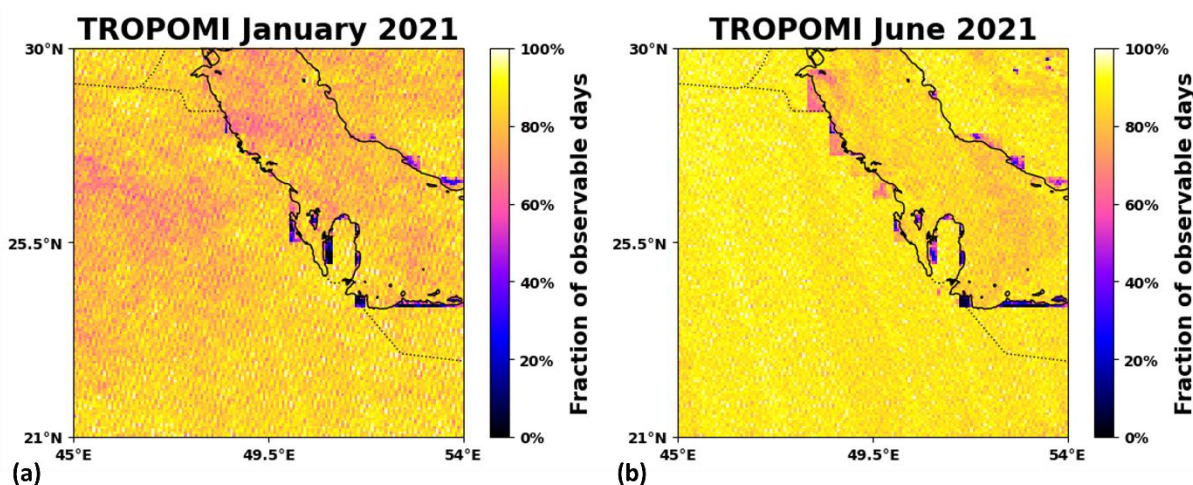
Figure 7: Fractions of good quality (qa>0.75) TROPOMI observations for each grid point of the nested domain (Figure 1) for
215 **January 2021 (a) and June 2021 (b).**

3. Results

3.1 Impact of chemistry in WRF-Chem simulations

In order to evaluate the role of the chemical processes impacting NO_2 (production/destruction rates, and NO-to-NO_2 conversion

220 rate), we carried out WRF-Chem simulations without the chemistry module for the period 1 to 10 June 2021 (NO and NO_2 were both considered as passive tracers). According to existing literature, the NO-to-NO_2 conversion that occurs via oxidation by ozone (e.g. Hanrahan, 1999; Atkinson 2000; Seinfeld and Pandis 2006) is often assumed to be instantaneous. We used the same model set-up as Section 2.1, however, for the passive tracer run, the EDGAR htap v2.2 NO_x input emissions were distributed as 90 % NO_2 and 10 % NO, contrary to the full chemistry run where NO_x was distributed as 90 % NO and 10 %

225 NO_2. The partitioning in NO_x emissions in the full chemistry run has been used in several previous studies (e.g. Solazzo et al.,

2017; Visser et al, 2019), while the high fraction of NO$_2$ in the no-chemistry run (90 %) has been used in recent studies to compensate for the absence of short-term conversion of NO-to-NO$_2$ (e. g. Kuhn et al, 2023; Xiang et al, 2022).

We compared the variations of NO$_2$ and NO concentrations as a function of the distance to an intense localized source, using both simulations (with and without chemistry), focusing on the isolated plume coming from the city of Riyadh. In Fig. 8, we

230   show the sum of the NO$_2$ concentrations over the tropospheric column depicted as the average of the 10-day period in June at 00:00 and 10:00 UTC (Fig. 8, panels a,b, e, and f). Similarly, we show the sum of the NO concentrations over the same area for the same period (Figures 8, panels c, d, g, and h). In the no-chemistry run, the NO$_2$ plumes display higher concentrations and extend further spatially, especially near the source compared to the chemistry run. The background NO$_2$ concentration is also higher in the no-chemistry run. Inversely, NO concentrations are higher in the full chemistry run compared to the no-

235   chemistry simulation, due to their low assumed fraction in total NO$_x$.
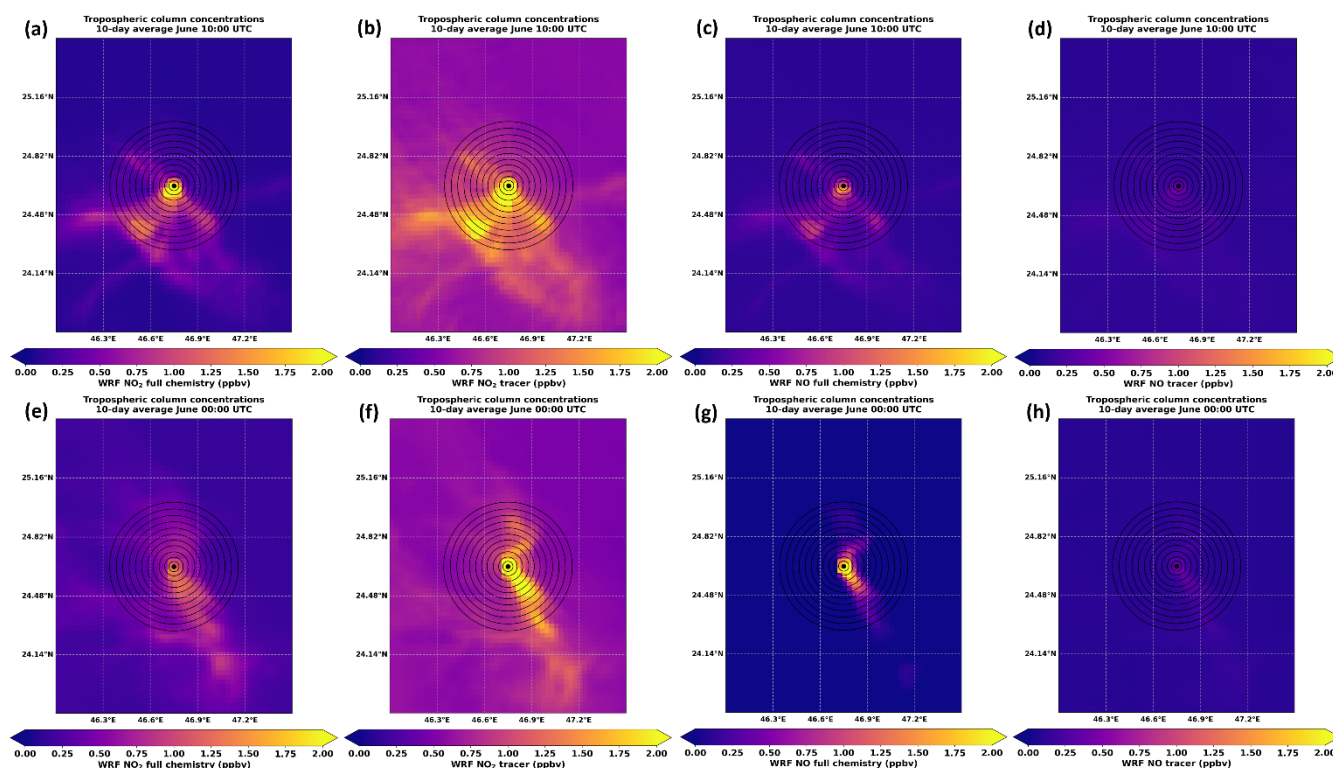
Figure 8: WRF-Chem simulated NO$_2$ (a,b, e, f) & NO (c, d, g, h) tropospheric column concentrations averaged for the period 1-10 June 2021 at 00:00 & 10:00 UTC with the highlighted point source and the distances (rings) for the run with the full chemistry activated and the only tracers run.

240   We show in Fig. 9 the sum of the concentrations within each ring (shown in Fig. 8) apart by 3 km, representing the evolution of both gases against the distance from the source. As shown in Fig. 8, the WRF-Chem model instantaneously converted NO to NO$_2$ during daytime (low NO concentrations). For the full chemistry simulations, the NO$_2$ and NO concentrations became almost null 40 km away from the point source due to the formation of O$_3$, whereas for the passive tracers simulation, the NO$_2$

concentrations remain significant even 57 km away from the source leading to a 200 % mismatch between the two
245 configurations. At night, the NO concentrations near the point source are higher when the chemistry is activated due to the
lack of incoming radiation, reducing further the NO-to-NO_2 conversion rate. However, as the lifespan of NO is much shorter
compared to NO_2, we noticed that the NO_2 concentrations became higher than NO starting from 9 km away from the source.
Next to the source (large emissions of NO and VOC), NO is converted to NO_2 to form O_3 in the presence of sunlight. Another
important reaction is the titration of O_3 by NO to form NO_2, which is converted to HNO_3, later removed by wet and dry
250 deposition processes. This reaction is especially important during the night when there is no photolytic reaction with NO_2, and
O_3 levels are the lowest as we can see near the point source in Fig. 9. However, as the plume moves further downwind, less
NO is available to react with O_3. Consequently, there is less O_3 degradation and O_3 levels increase as shown in Fig. 9. The
mismatch (up to 300%) during daytime between NO_2 from full chemistry simulations and NO_2 modeled as a tracer (no
chemistry) is mainly due to the formation of secondary pollutants (e.g. O_3) in the full chemistry simulation, confirming that
255 this reaction is clearly an important process when considering large point sources (e.g. power plants). The only sinks for the
NO and NO_2 tracers are the deposition processes. The anticorrelation between O_3 and NO_x for the Saudi Arabia region was
also observed via in-situ measurements in the area during 2007 (Butenhoff et al, 2015). Lama et al. (2022) have simulated NO_2
as a tracer with the WRF-Chem model for the period June to October 2018 over the city of Riyadh. Their modeled average
values of the tropospheric column concentrations for NO_2 at 10:00 UTC range from 1.4 to 0.4 ppbv, similar to the NO_2
260 concentration values we observed in our full chemistry simulation ranging from 2.2 ppbv above the source to 0.2 ppbv 60 km
away from the source (cf. Fig. 9(c)).
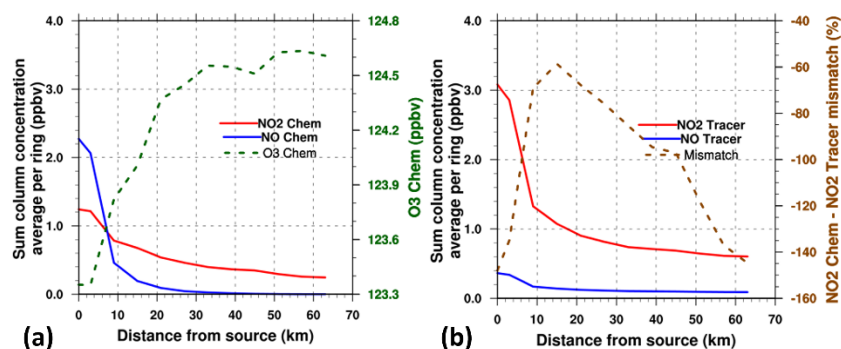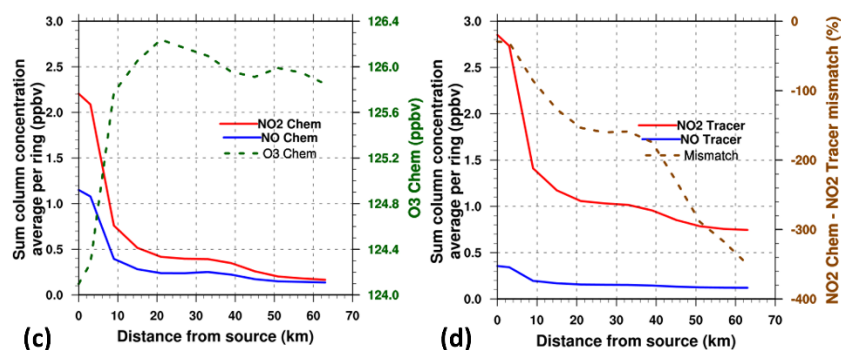
Figure 9: Comparison of 10-day average sum of the NO₂ and NO concentrations, including O₃ and the NO₂ mismatch between the full chemistry (left column) and the tracer (or no chemistry) run (right column), at 00:00 (a-b) and 10:00 (c-d) UTC in June as a function of distance from the source.

3.2 Comparison of satellite TROPOMI observations and WRF-Chem simulation

We compared the NO₂ tropospheric column concentrations from TROPOMI and from our WRF-Chem simulations using the full chemistry scheme for the months of January and June 2021 (cf. Fig. 10). More particularly, we compared the average value for the months of January and June 2021 at approximately 10:00 UTC for the nested domain of the simulation after regridding the WRF outputs to the TROPOMI observations and applying the same averaging kernel to the vertical levels. A Gaussian filter has also been applied in order to avoid some of the background noise (Goldberg et al, 2019; Goudar et al, 2023). During the month of January, the quality of the observations was frequently subpar, as seen in Fig. 7 but the overall coverage remains sufficient to evaluate the model-data mismatches over the entire month.
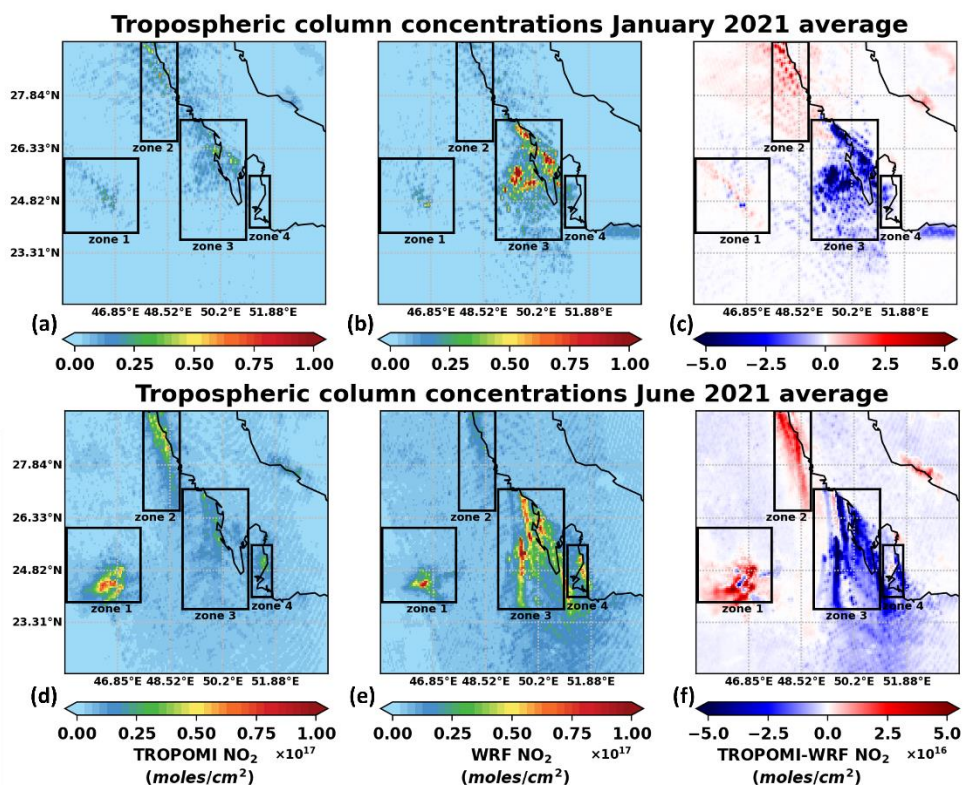
Figure 10: Tropospheric column NO₂ concentrations for the TROPOMI observations and the WRF-Chem outputs, alongside their concentration difference, monthly average for January 2021 (a-b-c) and June 2021 (d-e-f) at 10:00 UTC.

As we can see from Fig. 10, there is not a good agreement between the satellite data and the modeled concentrations regarding the location of the point sources (upwind of the plumes). Nevertheless, the sizes and intensity of the plumes of NO₂ vary across the different regions. Over the coastal capital city of Qatar, Doha (zone 4), the modeled concentrations in the plume are about 1.5-2 times higher than the observed TROPOMI values. Similarly, for the nearby coastal cities of Saudi Arabia (Dammam and Al-Jubail) and further away from the coast (Al-Hofuf, zone 3), the NO₂ concentration values for the model are much higher compared to the satellite observations. In the northern part of the domain, the coastal area of Saudia Arabia shows a more intense plume with concentrations two times higher in the satellite observations compared to the WRF-Chem model values (zone 2). The last noticeable plume is located over the western part of the domain, where the city of Riyadh is located (zone 1), with a wider and more intense plume in TROPOMI observations. We also note a secondary plume in TROPOMI data, south of the main one, which is not observed in the model.

In Fig. 11, we present a direct comparison of NO₂ concentrations between the satellite observations and the model, separated into four distinct zones (as described above). We selected these boxes as they include isolated plumes separable from other sources and estimated the sum of the 80th percentile concentrations for the tropospheric column (raw values - no Gaussian filtering) for each day of June and January 2021. The model-data correlations are larger for zone 1 despite the presence of a

secondary plume in this region (observed by TROPOMI but not by WRF-Chem) which suggests an overestimation of the modeled plume concentrations by the unique point source in Riyadh. For zone 2, the NO_2 concentrations were systematically underestimated by the model (1.5-2 times lower), whereas for zones 3 and 4 the WRF-Chem model overestimated the concentrations by a factor of 3-4 during both January and June 2021.
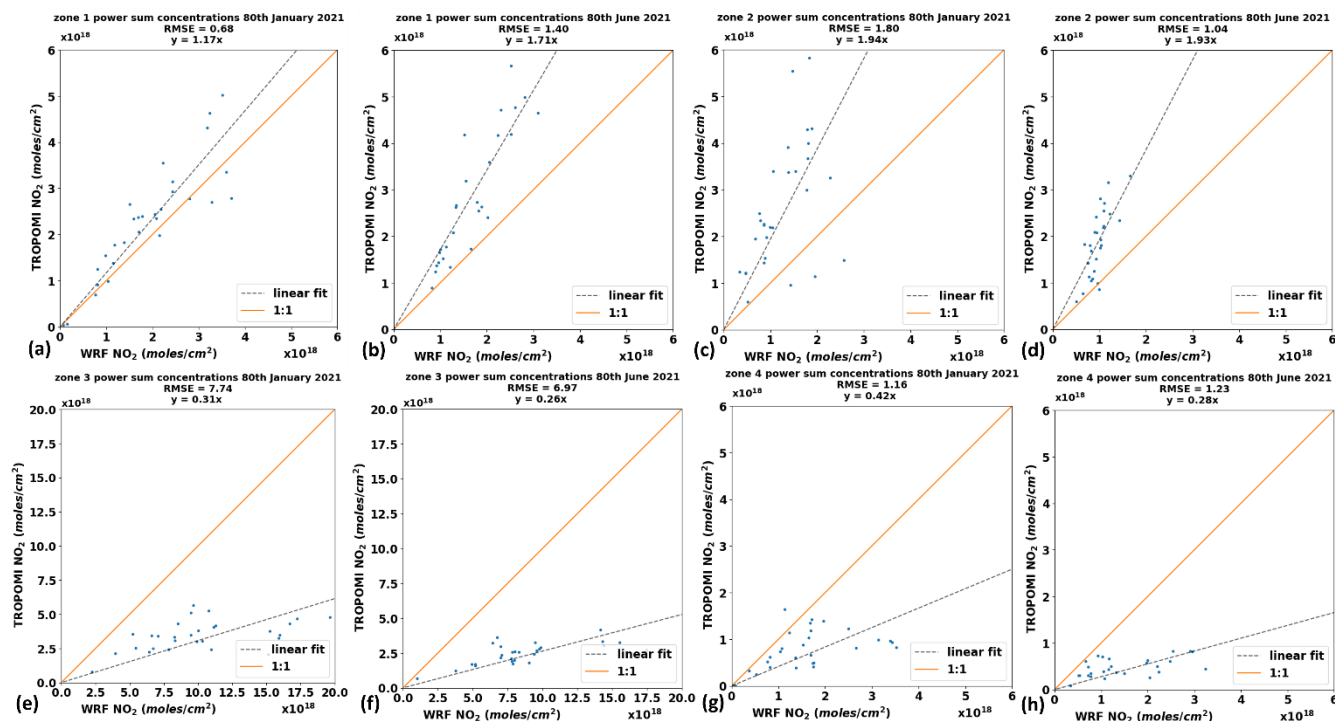
295

Figure 11: Comparison of the total column NO_2 concentrations for the four zones (cf. Figure 10) for each day of January (a-c-e-g) and June (b-d-f-h) at 10:00 UTC, including the corresponding linear regression (dashed line; principle of least squares).

In order to examine whether the model performances correspond to an overall underestimation or overestimation of the emissions, we applied the emissions scaling factors (in this case the slope of the linear fit) to the EDGAR emissions for the 4
300 zones separately and we summed the values for each, thus estimating the scaling factors for the sum. We know that this approach assumes linearity in the emission-to-concentration relationship, which is clearly not correct at the daily timescale. Sensitivity runs would be needed to define the impact of nonlinear chemical processes. However, the results presented in Table 2 suggest a large overestimation of the emissions, of about 2.5 times for both June and January, which is much larger than potential nonlinear reactions over the whole time period. Future studies should also include the nonlinear impacts of chemical
305 reactions to quantify more accurately the NO_2 emissions, but our findings confirm the presence of large discrepancies between the EDGAR inventory (established for the year 2010) and the observed plumes at sub-national scale.

Table 2: EDGAR NOₓ emissions per zone including applied emission scaling factor as occurred by the TROPOMI vs WRF plot slope.

	Total NOₓ emissions (monthly average)			
	EDGAR (June) (moles cm⁻²)	*EDGAR (January) (moles cm⁻²)*	*EDGAR · slope Fig. 11 (June) (moles cm⁻²)*	*EDGAR · slope Fig. 11 (January) (moles cm⁻²)*
Zone 1	28562	28202	48841	32996
Zone 2	4203	4136	8112	8024
Zone 3	176173	153122	45805	47468
Zone 4	20868	24026	5843	10091
All zones (sum)	229806	209486	108601	98579
Scaling factor of sum	0.47	0.47		

310

3.3 Satellite and WRF-Chem enhancement ratios comparison

We now examine the performance regarding both NO_2 and CO_2 in plumes from large sources, more specifically the enhancement ratios (δNO_2:δXCO_2) in plumes between the WRF-Chem simulation and the satellite observations. For this purpose we carried out simulations with CO_2 as a passive tracer for June and January 2021 using the EDGAR v 6.0 GHG

315 anthropogenic emissions as introduced in Section 2.2. Fig. 12 shows the modeled tropospheric column XCO_2 plumes over the nested domain as simulated by the WRF-Chem model. The locations of the CO_2 plumes ressemble the simulated NO_2 plumes (cf. Fig. 6) as we focus here on a region dominated by anthropogenic sources. Biogenic fluxes in desertic areas remain low compared to fossil fuel sources, especially over the Middle East where large point sources drive the observed XCO_2 gradients.
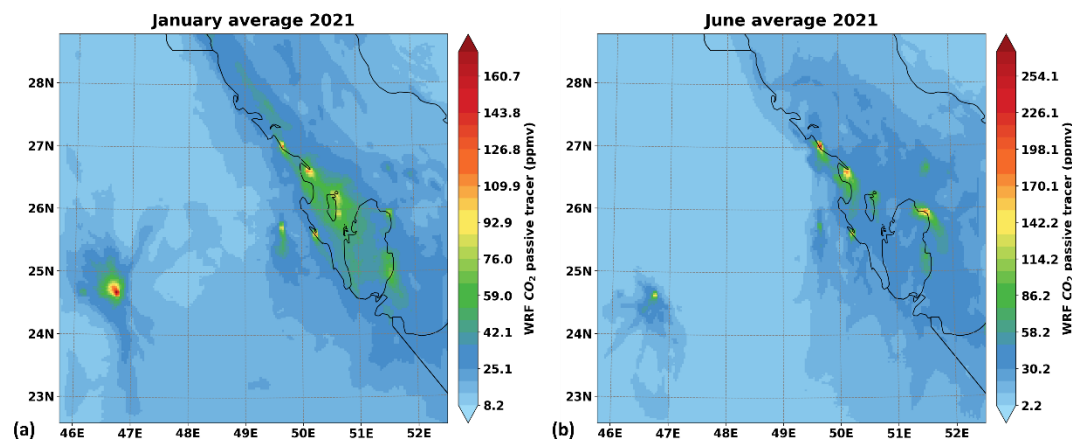
320 **Figure 12: Tropospheric column CO_2 concentrations for the WRF-Chem outputs monthly average for January 2021 (a) and June 2021 (b) at 10:00 UTC.**

For the quantification of the enhancement ratios, we applied the method described in Macdonald et al. (2022) summarized here. The plume corresponds to the 80th percentile of the NO_2 concentration in each subregion (zones), consequently masked while the remaining field is considered as background. To avoid missing retrievals, the masked area was filled in using the

325   nearest-neighbor interpolation technique and the resulting background field was subtracted from the plume values in order to obtain the enhancement fields δNO_2 and δXCO_2. Fig. B1 and B2 show each step of the method for the TROPOMI and OCO-3 data respectively over the urban area of Riyadh. The TROPOMI satellite data were regridded to the model resolution and the units were converted from moles cm^{-2} to ppb. The same method was applied to the WRF outputs for the same days.

Due to the scarcity of OCO-3 observations and the asynchronous sampling times of TROPOMI and OCO-3, we identified only

330   6 coincidental images over the time period, with 4 images for the urban area of Riyadh and 2 images for the urban area of Dammam. Fig. 13 shows two examples of observed and modeled δNO_2 and δXCO_2 plumes. Despite the plumes being correctly oriented in the WRF-Chem simulations, their widths appear lower than observed, for both TROPOMI and OCO-3. Considering that both gases are impacted by the same error, we suspect that transport model errors are responsible for the mismatch (wind speed, vertical mixing, or stability conditions) or the activity data used in EDGAR to map emissions are not diffused enough.

335   We decreased the potential impact of transport errors in our analysis by focusing on the integral over each plume, limiting the mislocation errors (due to incorrect wind speed and direction) that would affect a pixel-based analysis of the plumes. Here, the enhancement ratios were estimated based on the average value over the plume area.
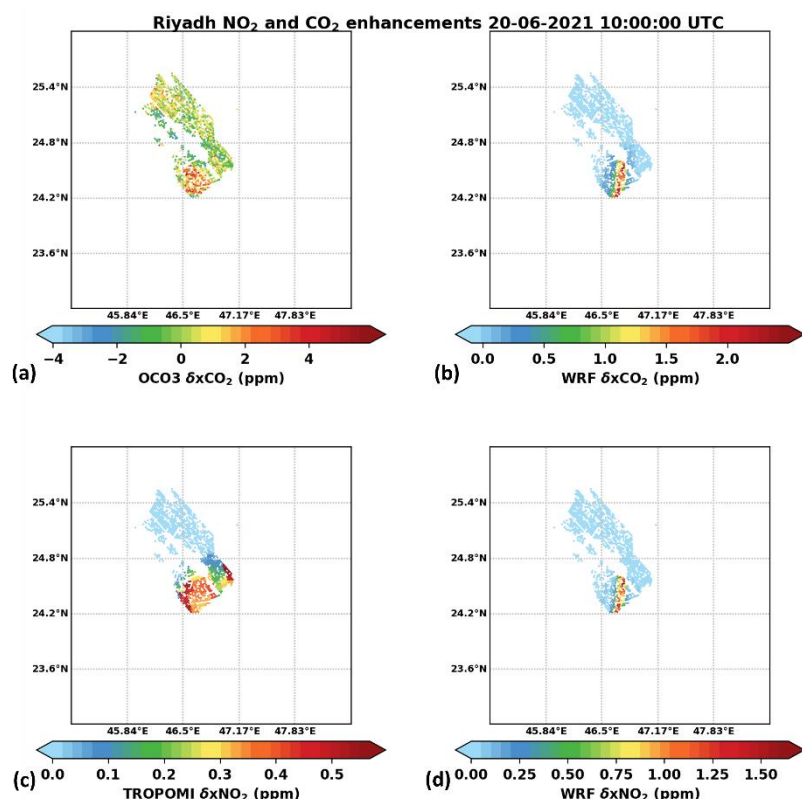
Figure 13: XCO₂ enhancements estimated from the OCO-3 observations (a), XCO₂ enhancements estimated from the WRF-Chem
340 **simulations (b), NO₂ enhancements estimated from the TROPOMI observations (c) and NO₂ enhancements estimated from the**
WRF-Chem simulations (full chemistry) (d) for the same coordinates over Riyadh on 20-06-2021 at 10:00 UTC

The scatter plot of the WRF-Chem enhancement ratio values against the satellite (TROPOMI and OCO-3) is shown in Fig. 14.
The linear regression of the enhancement ratios between WRF-Chem and the satellite concentrations shows a relatively good
agreement (slope of 0.72; R^2 =0.56) but the limited number of coincidental images in the observations limits the interpretation
345 of our analysis. We note here that the 0.72 value of the slope is similar to enhancement ratios over large urban areas observed
by MacDonald et al (2022) where the enhancement ratio values ranged from 0.5 ppb:ppm to 1.5 ppb:ppm and close to ratios
over Mexico City with 0.55 ppb:ppm dominated by traffic and large industry sources (Lei et al., 2022). We also note one
outlier with a high δXCO_2 relative to the δNO_2 enhancement (three times higher) corresponding to the 02/06/2021 case over
the city of Dammam despite having fair weather conditions during that day. More interestingly, we note that the overestimation
350 of δNO_2 enhancements in WRF-Chem (cf. Table 2) also applies to δXCO_2 values, resulting in a reasonable agreement in
δNO_2:δXCO_2 ratios. Despite the limited number of available observations (due to limited sampling by OCO-3), this
preliminary analysis confirms that potential biases in the EDGAR inventory affect both gases, confirming that a joint
assimilation of these two species can potentially rely on existing gas-to-gas ratios from EDGAR. We conclude here that

assimilating satellite observations of both NO_2 and CO_2 has the potential to improve emissions estimates from anthropogenic

355 sources at sub-national scales.
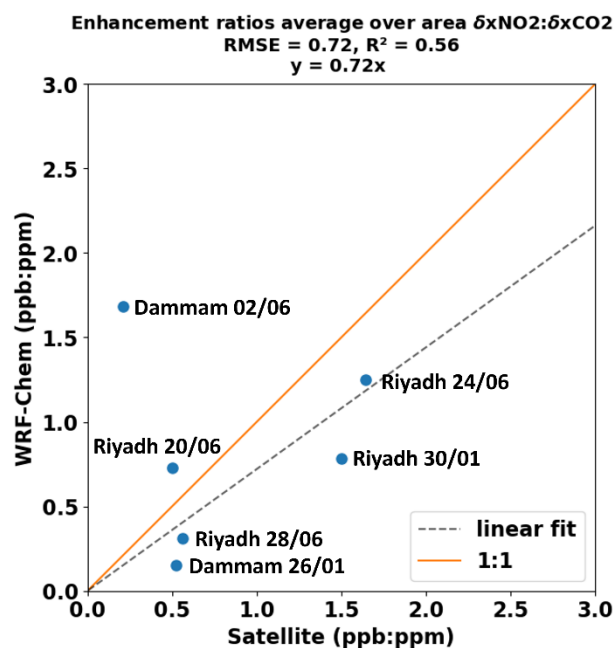
Figure 14: Comparison of the daily mean enhancement ratios (δNO₂:δXCO₂) from the WRF-Chem simulations and the TROPOMI observations over the six days with available satellite observations

Conclusions

360 As we demonstrated here, the abundance of satellite NO_2 concentrations from TROPOMI offers a unique set of observations for the quantification of NO_2 emissions and possibly for CO_2 emissions from large point sources or cities. An accurate representation of the NO_2 concentrations could lead to the quantification of the CO_2 emissions based on the known enhancement ratios δNO₂:δXCO₂ from existing inventories. In this manner, we used WRF-Chem simulations in order to examine the chemistry impact of the model regarding NO_x, to examine the performance of the EDGAR inventory, although it

365 is only available for the year 2010, and to evaluate the model performances regarding the enhancement ratios. In particular, we selected the Middle East as our study area for multiple reasons (distinct plumes from power plants, low cloud cover, low vegetation and a nearly-constant albedo) which are ideal for satellite observations in general (here TROPOMI and OCO-3). We carried out simulations for June and January 2021 for three different cases: 1) full chemistry, 2) NO_2 and NO as passive tracers, and 3) CO_2 as a passive tracer.

370 The first step was the examination of the chemistry module performances (cbm-z scheme). We performed 10 days of WRF-Chem simulation for June 2021 with full chemistry applied and one with NO_2 and NO as tracers. By comparing the NO_2 and NO concentration with the distance from a point source over Riyadh, we showed that the full chemistry is required to achieve

realistic representation of NO_2 concentrations at short and long distances from the source. The NO_2 and NO concentrations are almost neglected around 40 km away from the source for a full chemistry run, whereas NO_2 concentrations remain significant

375 even 60 km away for the tracers run. During the day, the mismatch in NO_2 concentrations between the full chemistry and the no-chemistry simulations reached up to 300% due to the absence of O_3 chemistry and despite the attribution of 90 % of the NO_x emissions to NO_2 emissions (to compensate for the absence of NO_2-to-NO conversion processes). During the night, when there is no incoming radiation, the NO_2 model-data mismatch reached up to 200 % near the source while decreasing further downwind (around 40 km away from the source).

380 Based on our full-chemistry configuration, we performed WRF-Chem simulations for the full months of January and June 2021. Our results confirmed the ability of the WRF-Chem model to represent the largest plumes over the Middle-East emitted by power plants. Furthermore, the locations of the plumes were in agreement with the satellite observations, despite transport model errors affecting the length and the width of the plumes. We defined four zones with large and distinct plumes in order to perform a spatial comparison with the TROPOMI satellite observations. The comparison revealed an underestimation of the

385 NO_2 concentrations by the model of approximately 1.5-2 times for two zones and an overestimation of 3-4 times for the other two. By applying the specific scaling factors to the raw emissions for these four zones (linearity assumption) and summing them, we derived an overall overestimation by the EDGAR inventory equivalent to a factor of 2.5.

Finally, we simulated the CO_2 enhancements with WRF-Chem for June and January 2021. The estimation of the enhancement ratios showed values of approximately 0.7, which agrees with other relevant studies (e. g. Macdonald et al., 2022; Lei et al.,

390 2022). Similar to the analysis of the NO_2 concentrations showing positive and negative corrections of the NO_2 emissions, the CO_2 model-data mismatches (OCO-3 retrievals) also showed similar mismatches. Despite the limited number of coincidental images of TROPOMI and OCO-3, we showed here that inconsistencies in sub-national CO_2 emissions in current global inventories might be corrected using NO_2 retrievals from TROPOMI. For future work, a detailed infrastructure map for the region could be taken into account to redistribute the anthropogenic emissions in a more realistic way, and the representation

395 of nonlinear chemical processes to establish more accurately the relationship between emissions and concentrations. Future inverse studies of CO_2 emissions will assimilate jointly NO_2 and XCO_2 satellite observations, taking into account the full complexity of chemistry reactions affecting NO_2, to produce monthly estimates over favorable regions (low cloud cover and reduced biogenic contribution).

Appendix A

400 **Table A1**

WRF-Chem input	EDGAR	WRF-Chem input	EDGAR
CO	CO	KET	0.0175·NMVOC
NO_x	0.9*NO	ORA2	0.0017·NMVOC

NO_x	$0.1*NO_2$	OLI	$0.037 \cdot NMVOC$
SO_2	SO_2	OLT	$0.04 \cdot NMVOC$
NH_3	NH_3	ETH	$0.0198 \cdot NMVOC$
ECJ(a)	$0.8*BC$	OL2	$0.0545 \cdot NMVOC$
ECI(a)	$0.2*BC$	CSL	$0.0019 \cdot NMVOC$
ORGJ(a)	$0.8*OC$	HCHO	$0.0137 \cdot NMVOC$
ORGI(a)	$0.2*OC$	ALD	$0.0071 \cdot NMVOC$
PM25I(a)	$0.2*PM2.5$	HC3	$0.142 \cdot NMVOC$
PM25J(a)	$0.8*PM2.5$	HC5	$0.1248 \cdot NMVOC$
PM_10(a)	PM10	HC8	$0.1565 \cdot NMVOC$
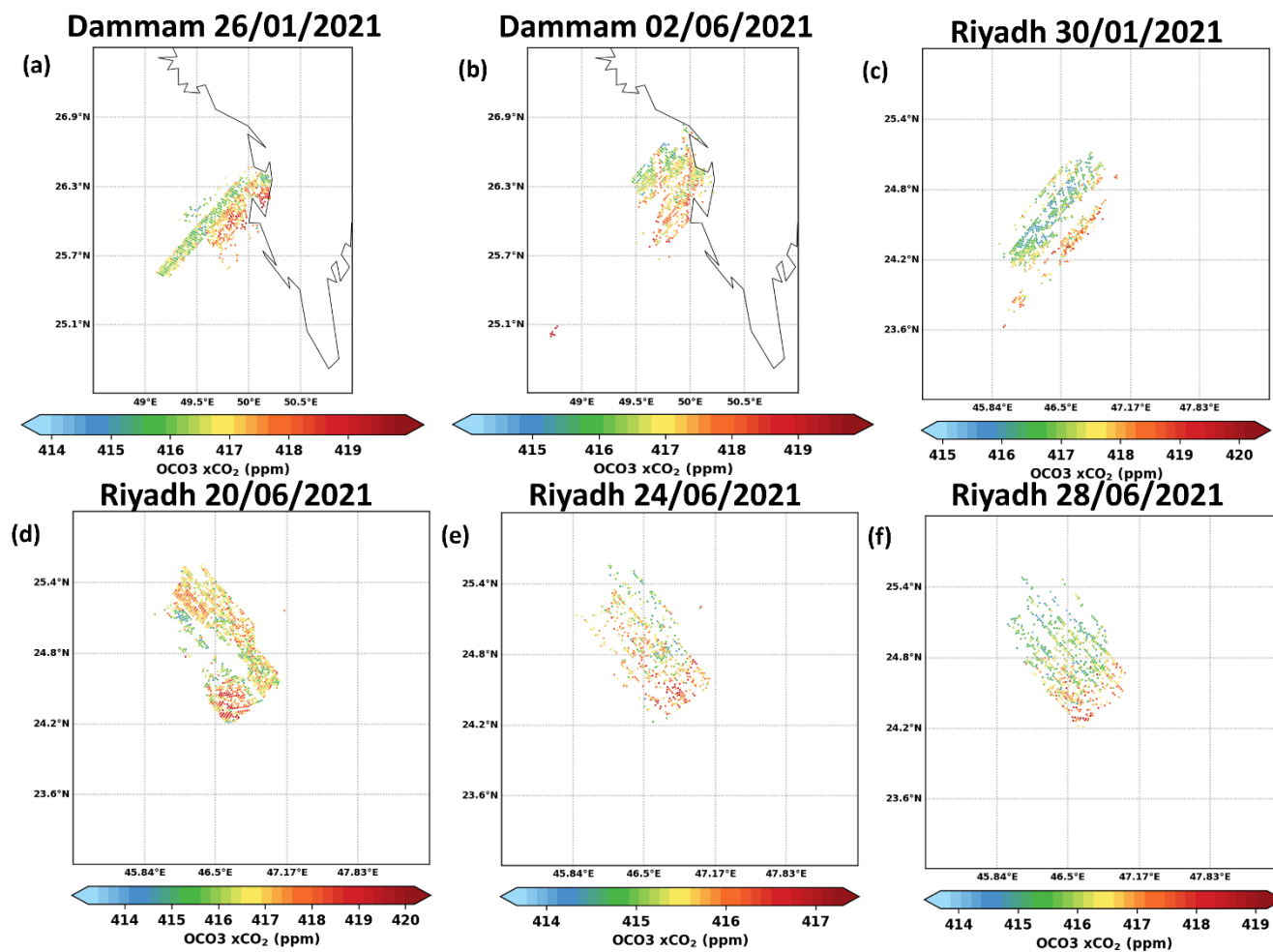
Figure A1: XCO2 retrievals (in ppmv) collected by OCO-3 in SAM mode over the cities of Riyadh (c-f) and Dammam (a-b) during the months of January and June 2021.

405 **Appendix B**
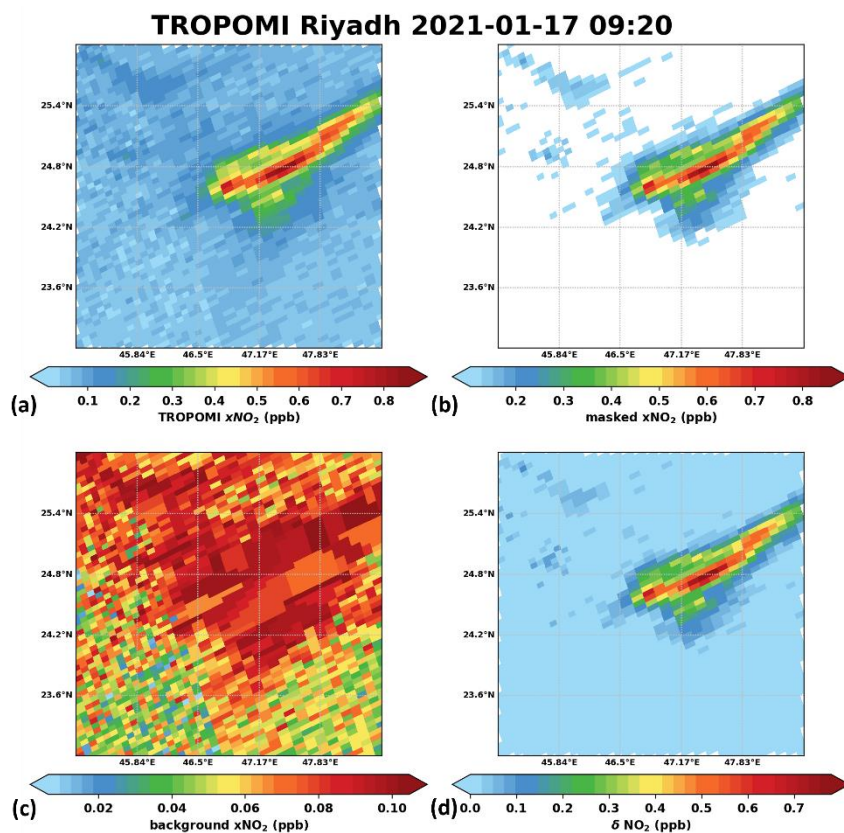
Figure B1: TROPOMI tropospheric column NO₂ concentration (a), 80th percentile of the TROPOMI tropospheric column NO₂ concentration (b), background noise after masking the 80th percentile of NO₂ concentrations and applying the nearest neighbor method to fill the grid points (c) and the enhancement ratio δxNO₂ after removing the background noise from the raw observations
410 (d) over Riyadh region on 14/01/2021 at 10:16 UTC
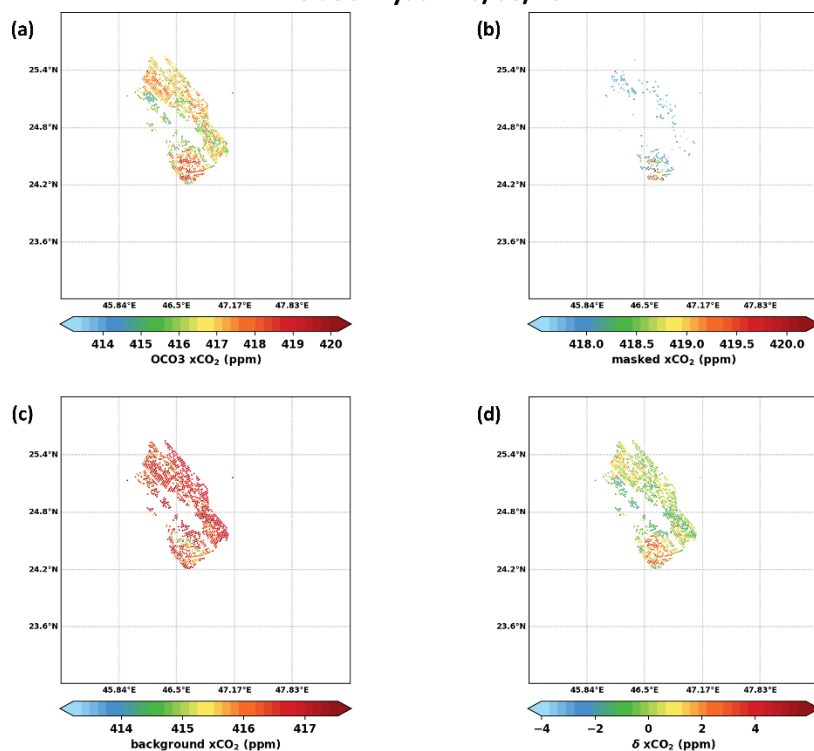
Figure B2: OCO3 tropospheric column CO₂ concentration (a), 80th percentile of the OCO-3 tropospheric column CO₂ concentration (b), background noise after masking the 80th percentile of CO₂ concentrations and applying the nearest neighbor method to fill the grid points (c) and the enhancement ratio δxCO₂ after removing the background noise from the raw observations (d) over Riyadh region on 20/06/2021

Author contribution

IC, TL and PC conceptualized this study. IC ran the WRF-Chem simulations, processed the data and analyzed the results for all the parts of the study with the help of JL, TC, GG and TL regarding the model set-up and the help of PK, YK, RL, TL and PC regarding the analysis of the results. IC, TL and PC wrote the original draft with contributions from AB for Section 3.1. All authors participated in the review and editing of the manuscript and agreed to this version.

Competing interests

The authors declare that they have no conflict of interest.

Acknowledgements

This work is a contribution to the EU-Funded EMME-CARE research project (under grant no. 856612). The authors thank the
425 French Alternative Energies and Atomic Energy Commission and the Cyprus Institute for funding this project.

We acknowledge the use of Satellite data produced by the OCO-3 project at the Jet Propulsion Laboratory, California Institute of Technology, and obtained from the OCO-3 data archive maintained at the NASA Goddard Earth Science Data and Information Services Center.

The wind date were retrieved from the METAR archive of the Iowa Environmental Mesonet, Iowa State University,
430 https://mesonet.agron.iastate.edu/request/download.phtml?network=SA__ASOS, accessed on 23 October 2023.

The atmospheric emissions data were retrieved from the Joint Research Centre Data Catalogue, 2017 & 2021 updates, http://jeodpp.jrc.ec.europa.eu/ftp/jrc-opendata/EDGAR/datasets/, accessed on 23 October 2023.

References

Al Ghamdi, A.: Saudi Arabia energy report, King Abdullah Pet. Stud. Res. Cent., doi: 10.30573/ KS--2020-DP25, 2020.

435 Rey-Pommier, A., Chevallier, F., Ciais, P., Kushta, J., Christoudias, T., Bayram, I. S., and Sciare, J.: Detecting nitrogen oxide emissions in Qatar and quantifying emission factors of gas-fired power plants - A four-years study, EGUsphere [preprint], doi:10.5194/egusphere-2023-1024, 2023.

Atkinson, R., Atmospheric Chemistry of VOCs and NO_X, Atm. Env., 34, 2063-2101, doi:10.1016/S1352-2310(99)00460-4, 2000.

440 Butenhoff, C. L., Khalil, M. A. K., Porter, W. C., Al-Sahafi, M. S., Almazroui, M., and Al-Khalaf, A.: Evaluation of ozone, nitrogen dioxide, and carbon monoxide at nine sites in Saudi Arabia during 2007, J. Air Waste Man. Assoc., 65, 871–886, doi: 10.1080/10962247.2015.1031921, 2015.

Chen, F., and Dudhia, J.: Coupling an advanced land-surface/hydrology model with the Penn State/NCAR MM5 modeling system, Part I: Model description and implementation, Mon. Weather Rev., 129, 569–585, doi:10.1175/1520-
445 0493(2001)129<0569:CAALSH>2.0.CO;2, 2001.

Chevallier, F., Broquet, G., Pierangelo, C., and Crisp, D.: Probabilistic global maps of the CO2 column at daily and monthly scales from sparse satellite measurements, J. Geo. Res: Atmospheres, 122, 7614-7629, doi: 10.1002/2017JD026453, 2017.

Copernicus Sentinel-5P (processed by ESA): TROPOMI Level 2 Nitrogen Dioxide total column products Version 02, European Space Agency, doi:10.5270/S5P-9bnp8q8, 2021.

450 Crippa, M., Solazzo, E., Huang, G., Guizzardi, D., Koffi, E., Muntean, M., Schieberle, C., Friedrich, R., Janssens-Maenhout, G.: High resolution temporal profiles in the Emissions Database for Global Atmospheric Research, Sci. Data 7,1–17, doi:10.1038/s41597-020-0462-2, 2020.

Crisp, D., Pollock, H.R., Rosenberg, R., Chapsky, L., Lee, R.A.M., Oyafuso, F.A., Frankenberg, C., O'Dell, C.W., Bruegge, C.J., Doran, G.B., Eldering, A., Fisher, B.M., Fu, D., Gunson, M.R., Mandrake, L., Osterman, G.B., Schwandner, F.M., Sun,

455 K., Taylor, T.E., Wennberg, P.O., Wunch, D.: The on-orbit performance of the Orbiting Carbon Observatory-2 (OCO-2)
     instrument and its radiometrically calibrated products, Atmos. Meas. Tech., 10, 59–81, doi:10.5194/amt-10-59-2017, 2017.

     Elguindi, N., Granier, C., Stavrakou, T., Darras, S., Bauwens, M., Cao, H., Chen, C., Denier van der Gon, H. A. C., Dubovik,
     O., Fu, T. M., Henze, D. K., Jiang, Z., Keita, S., Kuenen, J. J. P., Kurokawa, J., Liousse, C., Miyazaki, K., Müller, J. F., Qu,
     Z., Solmon, F., and Zheng, B.: Intercomparison of magnitudes and trends in anthropogenic surface emissions from bottom-up

460 inventories, top-down estimates and emission scenarios, Earths Future, 8, e2020EF001520, doi:10.1029/2020EF001520, 2020.

     Eskes, H., van Geffen, J., Boersma, F., Eichmann, K.-U., Apituley, A., and Pedergnana, M.: Sentinel-5 Precursor/TROPOMI
     level 2 product user manual nitrogen dioxide (technical report nos. S5P-KNMI-L2-0021-MA, 4.1.0, 2.4.0, 2022-07-
     11), Neth. Inst. Sp. Res. (SRON), Retrieved from: https://sentinel.esa.int/documents/247904/2474726/Sentinel-5P-Level-
     2-Product-User-Manual-Nitrogen-Dioxide.pdf, 2022.

465 Fast, J. , D., Gustafson, W. I., Easter, R. C., Zaveri, R. A., Barnard, J. C., Chapman, E. G., Grell, G. A., and Peckham, S. E.:
     Evolution of ozone, particulates and aerosol direct radiative forcing in the vicinity of Houston using a fully coupled
     meteorology-chemistry-aerosol model, J. Geophys. Res., 111, D21305, doi:10.1029/2005JD006721, 2006.

     Friedlingstein, P., O'Sullivan, M., Jones, M.W., Andrew, R.M., Gregor, L., Hauck, J., Le Qu´er´e, C., Luijkx, I.T., Olsen, A.,
     Peters, G.P., Peters, W., Pongratz, J., Schwingshackl, C., Sitch, S., Canadell, J.G., Ciais, P., Jackson, R.B., Alin, S.R., Alkama,

470 R., Arneth, A., Arora, V.K., Bates, N.R., Becker, M., Bellouin, N., Bittig, H.C., Bopp, L., Chevallier, F., Chini, L.P., Cronin,
     M., Evans, W., Falk, S., Feely, R.A., Gasser, T., Gehlen, M., Gkritzalis, T., Gloege, L., Grassi, G., Gruber, N., Gürses, ¨O.,
     Harris, I., Hefner, M., Houghton, R.A., Hurtt, G.C., Iida, Y., Ilyina, T., Jain, A.K., Jersild, A., Kadono, K., Kato, E., Kennedy,
     D., Klein Goldewijk, K., Knauer, J., Korsbakken, J.I., Landschützer, P., Lef`evre, N., Lindsay, K., Liu, J., Liu, Z., Marland,
     G., Mayot, N., McGrath, M.J., Metzl, N., Monacci, N.M., Munro, D.R., Nakaoka, S.-I., Niwa, Y., O'Brien, K., Ono, T., Palmer,

475 P.I., Pan, N., Pierrot, D., Pocock, K., Poulter, B., Resplandy, L., Robertson, E., R¨odenbeck, C., Rodriguez, C., Rosan, T.M.,
     Schwinger, J., S´ef´erian, R., Shutler, J.D., Skjelvan, I., Steinhoff, T., Sun, Q., Sutton, A.J., Sweeney, C., Takao, S., Tanhua,
     T., Tans, P.P., Tian, X., Tian, H., Tilbrook, B., Tsujino, H., Tubiello, F., van der Werf, G.R., Walker, A.P., Wanninkhof, R.,
     Whitehead, C., Willstrand Wranne, A., Wright, R., Yuan, W., Yue, C., Yue, X., Zaehle, S., Zeng, J., Zheng, B.: Global Carbon
     Budget 2022, Earth Syst. Sci. Data 14, 4811-4900, doi: 10.5194/essd-14-4811-2022, 2022.

480 Georgiou, G. K., Christoudias, T., Proestos, Y., Kushta, J., Pikridas, M., Sciare, J., Savvides, C., and Lelieveld ,J.: Evaluation
     of WRF-Chem model (v3.9.1.1) real-time air quality forecasts over the Eastern Mediterranean, Geosci. Model Dev., 15, 4129–
     4146, doi:10.5194/gmd-15-4129-2022, 2022.

     Georgiou, G. K., Christoudias, T., Proestos, Y., Kushta, J., Hadjinicolaou, P., and Lelieveld, J.: Air quality modelling in the
     summer over the eastern Mediterranean using WRF-Chem: chemistry and aerosol mechanism intercomparison, Atmos. Chem.

485 Phys., 18, 1555–1571, doi:10.5194/acp-18-1555-2018, 2018.

     Goldberg, D. L., Lu, Z., Streets, D. G., de Foy, B., Griffin, D., McLinden, C. A., Lamsal, L. N., Krotkov, N. A., and Eskes,
     H.: Enhanced capabilities of TROPOMI NO2: estimating NO_x from North American cities and power plants, Environ. Sci.
     Technol., 53, 12594–12601, doi:10.1021/acs.est.9b04488, 2019.

Goldberg, D. L., Saide, P. E., Lamsal, L. N., de Foy, B., Lu, Z., Woo, J.-H., Kim,Y., Kim, J., Gao, M., Carmichael, G., and
490   Streets, D. G.: A top-down assessment using OMINO2 suggests an underestimate in the NO_x emissions inventory in Seoul,
South Korea, during KORUS-AQ, Atmos. Chem. Phys., 19, 1801–1818, doi:10.5194/acp-19-1801-2019, 2019.

Goudar, M., Anema, J. C., Kumar, R., Borsdorff, T., and Landgraf, J.: Plume detection and emission estimate for biomass
burning plumes from TROPOMI carbon monoxide observations using APE v1. 1, Geosci. Mod. Dev., 16, 4835-4852,
doi:10.5194/gmd-16-4835-2023, 2023.

495   Grell, G.A., Peckham, S. E., Schmitz, R., Mc Keen, S. A., Frost, G., Skamarock, W. C., and Eder, B.: Fully coupled "online"
chemistry within the WRF model, Atmos. Environ., 39, 6957–6975, doi:10.1016/j.atmosenv.2005.04.027, 2005.

Hakkarainen, J., Szela̧ M. E., Ialongo, I., Retscher, C., Oda, T., and Crisp, D.: Analyzing nitrogen oxides to carbon dioxide
emission ratios from space: A case study of Matimba power station in Africa, Atmos. Environ. X, 10, 100110,
doi:10.1016/j.aeaoa.2021.100110, 2021.

500   Hanrahan P. L.: The plume volume molar ratio method for determining NO_2/NO_x ratios in modeling—part I: Methodology. J
Air Waste Manag. Assoc., 49, 1324–1331, doi:10.1080/10473289.1999.10463960, 1999.

Hong, S., Noh, Y., and Dudhia, J.: A new vertical diffusion package with an explicit treatment of entrainment processes, Mon.
Weather Rev., 134, 2318–2341, doi:10.1175/MWR3199.1, 2006.

Janssens-Maenhout, G., Crippa, M., Guizzardi, D., Dentener, F., Muntean, M., Pouliot, G., Keating, T., Zhang, Q., Kurokawa,
505   J., Wankmüller, R., Denier van der Gon, H., Kuenen, J. J. P., Klimont, Z., Frost, G., Darras, S., Koffi, B., and Li, M.:
HTAP_v2.2:a mosaic of regional and global emission gridmaps for 2008 and 2010 to study hemispheric transport of air
pollution, Atmos. Chem. Phys., 15, 11411–11432, doi:10.5194/acp-15-11411-2015, 2015.

Judd, L. M., Al-Saadi, J. A., Szykman, J. J., Valin, L. C., Janz, S. J., Kowalewski, M. G., Eskes, H. J., Veefkind, J. P., Cede,
A., Mueller, M., Gebetsberger, M., Swap, R., Pierce, R. B., Nowlan, C. R., Abad, G. G., Nehrir, A., and Williams, D.:
510   Evaluating Sentinel-5P TROPOMI tropospheric NO_2 column densities with airborne and Pandora spectrometers near New
York City and Long Island Sound, Atmos.Meas.Tech., 13, 6113–6140, doi:10.5194/amt-13-6113-2020, 2020.

Kuhlmann, G., Brunner, D., Broquet, G., and Meijer, Y.: Quantifying CO_2 emissions of a city with the Copernicus
Anthropogenic CO_2 monitoring satellite mission, Atmos. Meas. Tech., 13, 6733–6754, doi:10.5194/amt-13-6733-2020, 2020.

Kiel, M. Eldering, A., Roten, D. D., Lin, J. C., Feng, S., Lei, R., Lauvaux, T., Oda, T., Roehl, C. M., Blavier, J-F., and Iraci,
515   L. T.: Urban-focused satellite CO_2 observations from the Orbiting Carbon Observatory-3: A first look at the Los Angeles
megacity, Remote Sensing of Environment, 258, 112314, ISSN 0034-4257, doi:10.1016/j.rse.2021.112314, 2021.

Kuenen, J., Dellaert, S., Visschedijk, A., Jalkanen, J.-P., Super, I., and Denier van der Gon, H.: CAMS-REG-v4: a state-of-
the-art high-resolution European emission inventory for air quality modelling, Earth Syst. Sci. Data, 14, 491–515,
doi:10.5194/essd-14-491-2022, 2022.

520   Kuhn, L., Beirle, S., Kumar, V., Osipov, S., Pozzer, A., Bosch, T., Kumar, R. and Wagner, T.: Modelling of tropospheric NO_2
using WRF-Chem with optimized temporal NO_x emission profiles derived from in-situ observations -- Comparisons to in-situ,

satellite, and MAX-DOAS observations over central Europe, EGUsphere 2023, 1-38, doi:10.5194/egusphere-2022-1473, 2023.

Lama, S., Houweling, S., Boersma, K. F., Aben, I., Denier van der Gon, H. A., and Krol, M. C.: Estimation of OH in urban
525   plumes using TROPOMI-inferred NO₂/CO. Atm. Chem. Phys., 22, 16053-16071, doi:10.5194/ACP-22-160532022, 2022.

Lei, R., Feng, S., Xu, Y., Tran, S., Ramonet, M., Grutter, M., Garcia, A., Campos-Pineda, M., and Lauvaux, T.: Reconciliation of asynchronous satellite-based NO₂ and XCO₂ enhancements with mesoscale modeling over two urban landscapes, Rem. Sens. Envir., 281, 113241, ISSN 0034-4257, doi:10.1016/j.rse.2022.113241, 2022.

Lorente, A., Folkert Boersma, K., Yu, H., Dörner, S., Hilboll, A., Richter, A., Liu, M., Lamsal, L. N., Barkley, M., DeSmedt,
530   I., Van Roozendael, M., Wang, Y., Wagner, T., Beirle, S., Lin, J. T., Krotkov, N., Stammes, P., Wang, P., Eskes, H. J., and Krol, M.: Structural uncertainty in air mass factor calculation for NO₂ and HCHO satellite retrievals, Atmos. Meas. Tech., 10, 759–782, doi:10.5194/amt-10-759-2017, 2017.

Luna, A., Navarro, H. and Moya, A.: SO₂ and NO₂ simulation and validation in Metropolitan Lima using WRF-Chem model, Int. J. Comp. Meth. Exp. Meas., 8, 135-147, doi:10.2495/CMEM-V8-N2-135-147, 2020.

535   MacDonald, C. G., Laughner, J. L., Hedelius, J. K., Nassar, R., Mastrogiacomo, J.-P., and Wunch, D.: Estimating enhancement ratios of nitrogen dioxide, carbon monoxide, and carbon dioxide using satellite observations, Atm. Chem. Phys., 23, 1–30, doi: 10.5194/acp-23-3493-2023, 2023.

Madronich, S.: Photodissociation in the atmosphere: 1. Actinic flux and the effects of ground reflections and clouds, J. Geo. Res., 92, 9740, doi:10.1029/jd092id08p09740, 1987.

540   Monforti Ferrario, F., Crippa, M., Guizzardi, D., Muntean, M., Schaaf, E., Lo Vullo, E., Solazzo, E., Olivier, J., Vignati, E.: EDGAR v6.0 Greenhouse Gas Emissions. European Commission, Joint Research Centre (JRC) [Dataset] PID: http://data.europa.eu/89h/97a67d67-c62e-4826-b873-9d972c4f670b, 2021.

Monks, P. S., Archibald, A. T., Colette, A., Cooper, O., Coyle, M., Derwent, R., Fowler, D., Granier, C., Law, K. S., Mills, G. E., Stevenson, D. S., Tarasova, O., Thouret, V., von Schneidemesser, E., Sommariva, R., Wild, O., and Williams, M. L.:
545   Tropospheric ozone and its precursors from the urban to the global scale from air quality to short-lived climate forcer, Atm. Chem. Phys., 15, 8889–8973, doi:10.5194/acp-15-8889-2015, 2015.

Oda, T., Bun, R., Kinakh, V., Topylko, P., Halushchak, M., Marland, G., Lauvaux, T., Jonas, M., Maksyutov, S., Nahorski, Z., Lesiv, M., Danylo, O., and Horabik-Pyzel, J.: Errors and uncertainties in a gridded carbon dioxide emissions inventory, Mitig. Adapt. Strat. Gl., 24, 1007–1050, doi:10.1007/s11027-01909877-2, 2019.

550   Oda, T. and Maksyutov, S.: A very high-resolution (1km×1km) global fossil fuel CO₂ emission inventory derived using a point source database and satellite observations of night time lights, Atmos. Chem. Phys., 11, 543–556, doi:10.5194/acp-11543-2011, 2011.

O'Dell, C. W., Eldering, A., Wennberg, P. O., Crisp, D., Gunson, M. R., Fisher, B., Frankenberg, C., Kiel, M., Lindqvist, H., Mandrake, L., Merrelli, A., Natraj, V., Nelson, R. R., Osterman, G. B., Payne, V. H., Taylor, T. E., Wunch, D., Drouin, B. J.,
555   Oyafuso, F., Chang, A., McDuffie, J., Smyth, M., Baker, D. F., Basu, S., Chevallier, F., Crowell, S. M. R., Feng, L., Palmer,

P. I., Dubey M., García, O. E., Griffith, D. W. T., Hase, F., Iraci, L. T., Kivi, R., Morino, I., Notholt, J., Ohyama, H., Petri, C., Roehl, C. M., Sha, M. K., Strong, K., Sussmann, R., Te, Y., Uchino, O., and Velazco, V.A.: Improved retrievals of carbon dioxide from Orbiting Carbon Observatory-2 with the version 8 ACOS algorithm, Atmos. Meas. Tech., 11, 6539–6576, doi:10.5194/amt11-6539-2018, 2018.

560 Peylin, P., Law, R.M., Gurney, K.R., Chevallier, F., Jacobson, A.R., Maki, T., Niwa, Y., Patra, P.K., Peters, W., Rayner, P.J. and Rödenbeck, C.: Global atmospheric carbon budget: results from an ensemble of atmospheric CO_2 inversions, Biogeosci., 10, 6699-6720, doi:10.5194/bg-10-6699-2013, 2013.

Reuter, M., Buchwitz, M., Schneising, O., Krautwurst, S., O'Dell, C. W., Richter, A., Bovensmann, H., and Burrows, J. P.: Towards monitoring localized CO_2 emissions from space: collocated regional CO_2 and NO_2 enhancements observed by the
565 OCO-2 and S5P satellites, Atmos. Chem. Phys., 19, 9371–9383, doi:10.5194/acp-19-9371-2019, 2019.

Roten, D., Lin, J. C., Kunik, L., Mallia, D., Wu, D., Oda, T., and Kort, E. A.: The Information content of dense carbon dioxide measurements from space: A high-resolution inversion approach with synthetic data from the OCO-3 instrument, Atmos. Chem. Phys. Discuss. [preprint], https://doi.org/10.5194/acp-2022-315, in review, 2022.

Seinfeld, J. H. and Pandis, S. N.: Atmospheric chemistry and physics: From air pollution to climate change, Third edition,
570 John Wiley, New York, 2006.

Sicard, P., Crippa, P., De Marco, A., Castruccio, S., Giani, P., Cuesta, J., Paoletti, E., Feng, Z., and Anav, A.: High spatial resolution WRF-Chem model over Asia: Physics and chemistry evaluation, Atm. Env., 244, 118004, doi:10.1016/j.atmosenv.2020.118004, 2021.

Skamarock, W. C., and Klemp, J. B.: A time-split nonhydrostatic atmospheric model for research and NWP applications, J.
575 Comp. Phys., 227, 3465-3485, doi:10.1016/j.jcp.2007.01.037, 2008.

Smith, S. J., McDuffie, E. E., and Charles, M.: Opinion: Coordinated development of emission inventories for climate forcers and air pollutants, Atm. Chem. Phys., 22, 13201-13218, doi:10.5194/acp-22-13201-2022, 2022.

Solazzo, E., Bianconi, R., Hogrefe, C., Curci, G., Tuccella, P., Alyuz, U., Balzarini, A., Baró, R., Bellasio, R., Bieser, J., Brandt, J., Christensen, J. H., Colette, A., Francis, X., Fraser, A., Vivanco, M. G., Jiménez-Guerrero, P., Im, U., Manders, A.,
580 Nopmongcol, U., Kitwiroon, N., Pirovano, G., Pozzoli, L., Prank, M., Sokhi, R. S., Unal, A., Yarwood, G., and Galmarini, S.: Evaluation and error apportionment of an ensemble of atmospheric chemistry transport modeling systems: multivariable temporal and spatial breakdown, Atm. Chem. Phys., 17, 3001–3054, doi:10.5194/acp-17-3001-2017, 2017.

Stavrakou, T., Müller, J.-F., Boersma, K. F., Van Der A, R. J., Kurokawa, J., Ohara, T., and Zhang, Q.: Key chemical NO_x sink uncertainties and how they influence top-down emissions of nitrogen oxides, Atmos. Chem. Phys., 13, 9057–9082,
585 doi:10.5194/acp-13-9057-2013, 2013.

Taylor, T. E., O'Dell, C. W., Baker, D., Bruegge, C., Chang, A., Chapsky, L., Chatterjee, A., Cheng, C., Chevallier, F., Crisp, D. and Dang, L.: Evaluating the consistency between OCO-2 and OCO-3 XCO_2 estimates derived from the NASA ACOS version 10 retrieval algorithm, Atm. Meas. Tech., 16, 3173–3209, doi:10.5194/amt-16-3173-2023, 2023.

Tie, X., Madronich, S., Walters, S., Zhang, R., Rasch, P., and Collins, W., 2003, Effect of clouds on photolysis and oxidants
590   in the troposphere, Journal of Geophysical Research, 108, https://doi.org/10.1029/2003jd003659.

Visser, A. J., Boersma, K. F., Ganzeveld, L. N., and Krol, M. C.: European NO_x emissions in WRF-Chem derived from OMI:
impacts on summertime surface ozone, Atmos. Chem. Phys., 19, 11821–11841, doi:10.5194/acp-19-11821-2019, 2019.

WRF-Chem 3.9.1.1. Emissions Guide, 2018 Update, https://ruc.noaa.gov/wrf/wrf-chem/Emission_guide.pdf, accessed on 27
September 2023.

595   Wu, N., Geng, G., Yan, L., Bi, J., Li, Y., Tong, D., Zheng, B., and Zhang, Q.: Improved spatial representation of a highly
resolved emission inventory in China: Evidence from TROPOMI measurements. Env. Res. L., 16, 084056, doi10.1088/1748-
9326/ac175f, 2019.

Xiang, S., Zhang, S., Wang, H., Yu, Y.T., Wallington, T.J., Shen, W., Kirchner, U., Deng, Y., Tan, Q., Zhou, Z. and Wu, Y.:
Variability of NO_2/NO_x Ratios in multiple microenvironments from on-road and near-roadway measurements, ACS ES&T
600   Eng., 2, 1599-1610, doi:10.1021/acsestengg.2c00027, 2022.

Yang, E. G., Kort, E. A., Ott, L. E., Oda, T. and Lin, J. C.: Using space-Bbased CO_2 and NO_2 observations to estimate urban
CO_2 emissions, J. Geo. Res.: Atm., 128, doi:10.1029/2022JD037736, p.e2022JD037736,, 2023.

Yokota, T., Yoshida, Y., Eguchi, N., Ota, Y., Tanaka, T., Watanabe, H., and Maksyutov S.: Global concentrations of CO_2 and
CH_4 retrieved from GOSAT: first preliminary results, SOLA, 5, 160–163, doi:10.2151/sola.2009-041, 2009.

605   Yu, X., Millet, D. B., Henze, D. K., Turner, A. J., Delgado, A. L., Bloom, A. A. and Sheng, J.: A high-resolution satellite-
based map of global methane emissions reveals missing wetland, fossil fuel, and monsoon sources, Atm. Chem. and Phys., 23,
3325-3346, doi:10.5194/acp-23-3325-2023, 2023

Zaveri, R. A. and Peters, L. K.: A new lumped structure photochemical mechanism for large-scale applications, J. Geophys.
Res.Atmos., 104, 30387–30415, doi:10.1029/1999jd900876, 1999.

610   Zittis, G., Hadjinicolaou, P., and Lelieveld, J.: Comparison of WRF model physics parameterizations over the MENA-
CORDEX Domain, Am. J. Clim. Change, 3, 490–511, doi:10.4236/ajcc.2014.35042, 2014.